ADVANCED INTELLIGENT SYSTEMS
Open Access
www.advintellsyst.com

Bioinspired Multifunctional Mechanoreception of Soft–Rigid Hybrid Actuator Fingers

Shoulu Gong, Qifan Ding, Jiahao Wu, Wen-Bo Li, Xin-Yu Guo, Wen-Ming Zhang, and Lei Shao**

It is highly desired yet challenging to construct soft robots resembling the dexterous motor skills and powerful tactile sensations of human hands. Herein, a bioinspired design to create soft–rigid hybrid mechanoreceptive actuators (HMAs) and grippers is reported, imitating the musculoskeletal structure and embedded mechanoreception of human fingers, via careful ink preparation and a multimodality all-3D-printing technology. The HMAs consist of multiple rigid segments between joints, imitating phalanges, to mount flexible mechanoreceptive sensors in a flexible-on-rigid (FOR) design, yielding a bending-insensitive unambiguous mechanoreception. The printed sensors exhibit a humanoid high sensitivity for low contact force and a wide low-sensitivity linear detection range, combined with excellent long-term stability and low hysteresis. As a result, the HMA gripper not only shows greatly enhanced output force due to the soft–rigid hybrid design, but also enables multifunctional mechanoreceptive sensing including contact identification, gentle grabbing, and the estimation of size, weight, and stiffness of the grasped objects. This integrated approach of constructing soft robots with mechanoreception can provide a pathway toward feedback control, integrative biomimetic functions, and human–machine interface for all soft devices.

1. Introduction

Human hands are able to perform dexterous work, partially due to the complicated musculoskeletal system, and partially due to the delicate tactile sensation from numerous receptors and neurons inside skins. There have been lots of research effort in designing robotic counterparts but two key challenges still remain. One lies in the limitation that traditional stiff actuators are generally not compliant nor biologically compatible, and the other one is the lack of accurate and distributed tactile sensing ability. To overcome the first challenge, various soft actuators have been developed with better compliance, biocompatibility, and multimodal motions, leading to multiple attractive applications.[1–3] However, they are generally too compliant which limits their applications particularly in handling objects for industrial-grade grasping. There have been several methods to increase the stiffness of soft actuators,[4–6] such as using particle jamming,[7] shape memory alloys,[8] and tension reinforcement.[9] Recently, soft–rigid hybrid structures are proposed to improve the stiffness and robustness of soft actuators inspired by the human muscle–skeleton biomechanical structure,[10,11] resulting in a large output force together with considerable compliance. For example, L. Liu et al. utilized dielectric elastomers and skeleton backbone to design a soft–rigid hybrid actuators with large force and bending deformation,[12] among several other similar investigations.[13–15] Compared to the slow response of most stiffness-varying methods,[16–18] soft–rigid hybrid structures represent a closer imitation of the human musculoskeletal structure and also a faster and simpler solution.

The research attention has now also focused on the next-generation soft robots with integrated sensor systems to provide tactile sensing feedback using flexible electronics,[19,20] including mechanoreception, thermoreception, proprioception, etc. The use of flexible sensors is expected for improved compatibility with the large continuous deformation of soft actuators. In addition, arrays of sensor replica, or also known as electronic skins (e-skins), could provide a potential pathway to large-scale flexible sensor networks completely covering elastomer actuators and their based soft robots.[21,22] Numerous work has investigated the integration of different types of flexible sensors with soft robots for measuring pressure, curvature, strain, temperature, and so on.[23–25] Among them, triboelectric nanogenerator (TENG)-based sensors have attracted a lot of attention,[26,27]

S. Gong, Q. Ding, J. Wu, L. Shao
University of Michigan–Shanghai Jiao Tong University Joint Institute
Shanghai Jiao Tong University
Shanghai 200240, China
E-mail: lei.shao@sjtu.edu.cn

W.-B. Li, X.-Y. Guo, W.-M. Zhang
School of Mechanical Engineering and State Key Laboratory of Mechanical Systems and Vibration
Shanghai Jiao Tong University
Shanghai 200240, China
E-mail: wenmingz@sjtu.edu.cn

The ORCID identification number(s) for the author(s) of this article can be found under https://doi.org/10.1002/aisy.202100242.

DOI: 10.1002/aisy.202100242

which is based on the principle of electrostatic induction and contact electrification, and therefore the generated voltage due to charge transfer during contact and separation can be utilized to render contact pressure and motion information. For instance, J. Chen et al.[28] and S. Chen et al.[29] developed soft actuators integrated with triboelectric tactile sensors, and G. Yao et al.[30] developed a triboelectric e-skins for both pressure and proximity, while Y.-C. Lai et al.[31] developed a bioinspired triboelectric tactile sensor molded from microstructured leaves for pressure monitoring and texture identification. However, TENG-based tactile force sensors can only respond well to a fast transient force while not able to precisely track static or constant contact forces, as demonstrated by a mechanoreceptor based on a potentiometric–triboelectric hybridized sensing mechanism.[32] Therefore, they are not ideal to replicate the tactile feedback function of human skins, which are consisting of both fast and slow mechanoreceptors correspondent to transient contact (e.g., tapping and sliding) and static contact (e.g., continuous touch), respectively (**Figure 1**a). In addition, they are also known to be susceptible to external changes such as humidity and the texture and conductivity of the contacting objects, and also too sensitive to the operation conditions including the separation gap.

Moreover, Truby et al. fabricated a pneumatic soft actuator with integrated flexible inflation sensors, curvature sensors, and contact sensors using embedded 3D printing within a single mold for the actuator structure.[33] However, the piezoresistive contact sensors cannot provide accurate absolute force information[34,35] because it would respond to both actuator bending and contact pressure. There are still many other investigations which have proposed integration of single or multiple flexible sensors on soft actuators, such as tactile sensor arrays on a soft prosthetic hand[36] and strain sensors on a soft tentacle gripper[37] and so on, but nevertheless they all lack a clear pathway to decouple deformations from grasping forces. Although many bending-insensitive pressure sensors have been developed,[38–41] the mounting of these sensors on soft actuators could result in a local flexural deformation of the sensor and actuator material together when receiving contact pressure, resulting in ambiguous sensor response. These known problems of coupling in flexible sensors and integrative soft actuator–sensor structures seriously prevent their effective deployment.

Here, we report a method of creating bioinspired soft–rigid hybrid actuators carrying distributed flexible microstructured force sensors, imitating the joint–phalange biomechanical structure and also mechanoreceptors of human fingers as well, via an efficient multimodality all-3D-printing technology. These biomimetic actuators, referred to as soft–rigid hybrid mechanoreceptive actuators (HMAs) later, are consisting of a soft actuator body with discrete rigid bending retainers, which are fabricated by stereolithographic (SLA) printing, and flexible mechanoreceptive sensors on these retainers by inkjet printing and pneumatic direct ink writing (DIW). By harnessing a soft–rigid hybrid design of the actuating structures, it not only enhances the output force but also provides relatively rigid segments (between bending joints) for integrating flexible mechanoreceptive sensors in a flexible-on-rigid (FOR) design, so that there is no spurious response brought by actuator bending. Thus, the feedback from the sensors reflects the unambiguous contact pressure received at their particular locations on the actuator. By assembling these HMAs into a soft robotic gripper with distributed mechanoreceptors on different phalangeal segments along an actuator finger, we show multifunctional bending-insensitive mechanoreception with the capability of gentle grasps, contact identification, and the sensing of size, weight, and stiffness of the grasped objects. The achieved mechanoreception by multilocation contact detection of both transient and static touch with an unambiguous force or pressure level has not yet been realized by other soft actuators.

2. Results and Discussions

2.1. Ink Preparation and Multimodality 3D Printing

The HMAs consist of a specially designed soft–rigid hybrid pneumatic actuator, which is mainly composed of an inner soft latex tube and ring-shaped rigid frames (Rigid Frame 1, 2, and 3) with different lengths used to constrain radial expansion of the soft tube under inflation. In addition, a constrain layer (65Mn) is used to connect all rigid frames and restrict stretching at its side. The rigid top and pedestal frames are used to seal the soft tube and mount to the gripper base for pneumatic actuation, respectively. The actuator is assembled by inserting the soft tube through a combination of long and short rigid frames, for which the shorter ones imitate the flexible joints of human fingers like the distal interphalangeal (DIP) joint and the proximal interphalangeal (PIP) joint, while the longer ones imitate the rigid phalanges between joints and can be also used for embedding mechanoreceptive sensors. We note that the meaning of the soft–rigid hybrid design is twofolds, one referring to an assembly consisting of the inner soft tube and the outer rigid frames, while the other indicating the alternating flexible bending joints (Rigid Frame 1) and stiff bending retainers (Rigid Frame 2). These longer rigid frames will result in a discontinuous bending similar to human fingers, unlike typical fluidic elastomer actuators, as indicated by the blue connected line segments in Figure 1a,b. When inflated, the soft tube tends to elongate axially but restricted at the side having the constrain layer, leading to a bending deformation. Radial expansion, another result due to inflation, is not useful nor energy efficient for bending and is thus restricted by those rigid frames. All rigid frames and pedestals are fabricated with commercial UV-curing resin materials using SLA 3D printing, as shown in Figure 1c. The assembling of the actuator is shown in Figure 1d and the complete assembling process can be obtained in Section II, Supporting Information.

Figure 1b presents a prototype of the HMA with two capacitive-transduced mechanoreceptive sensors integrated on the surface of two pieces of Rigid Frame 2 separately. Thus, the bending of the sensors is minimized during actuator deformation, resulting in better accuracy and stability for force measurements. The capacitive sensors, mimicking mechanoreceptors on human fingers, are consisting of a soft silicone-based dielectric layer sandwiched between two silver nanoparticle conductive layers, which are wrapped inside flexible polyethylene terephthalate (PET) substrates. When there is applied pressure on the sensor, the dielectric layer is squeezed thinner so that the capacitance increases. Compared to triboelectric tactile force sensors used in soft actuators, the flexible mechanoreceptive sensors used in this work can

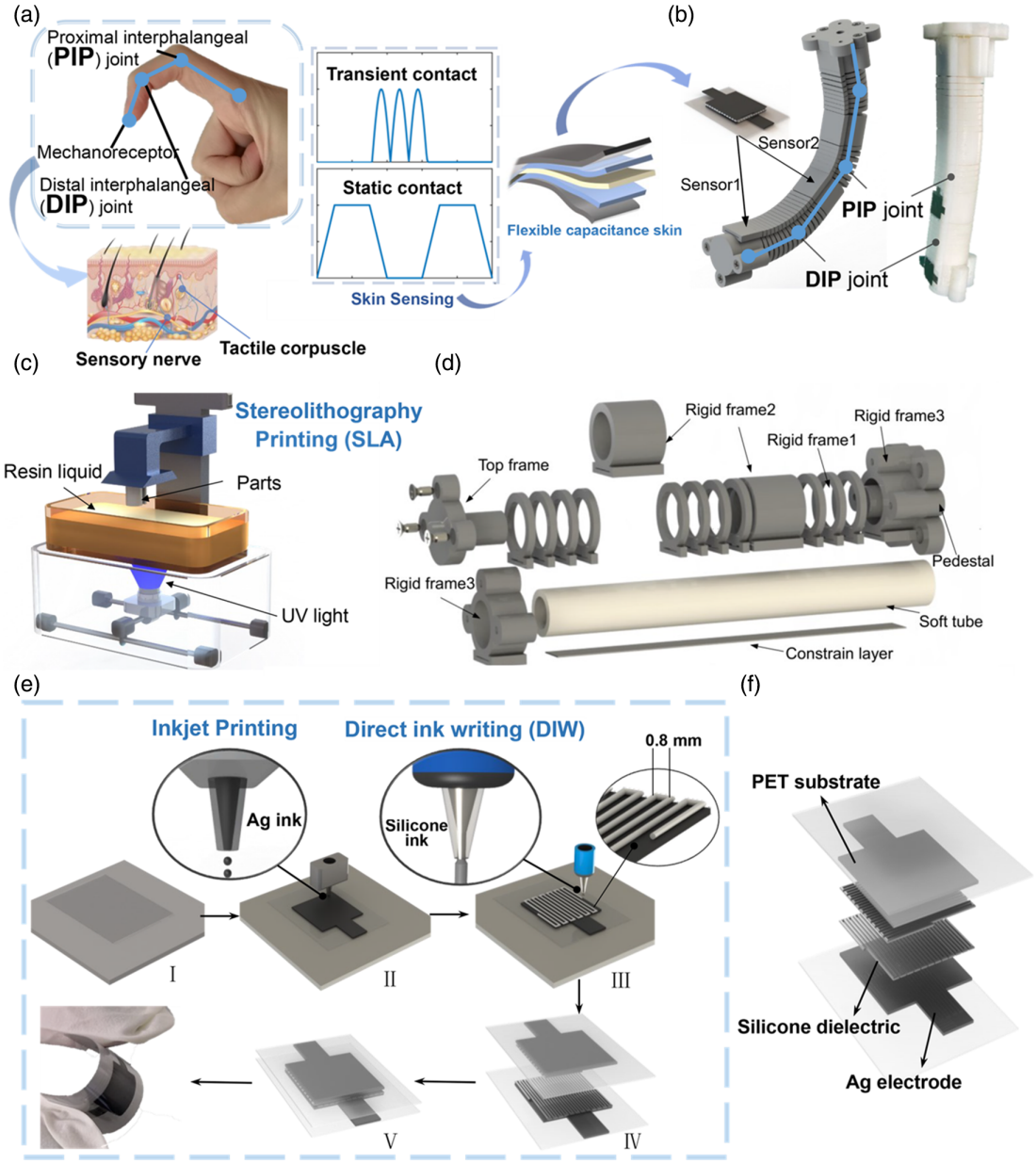

Figure 1. Fully printed soft–rigid hybrid mechanoreceptive actuators (HMAs) manufactured by multimodality 3D printing. a) Biomechanical joint–phalange structure of human fingers and mechanoreceptors underneath skins, with analogous flexible force sensors for the detection of both transient and static contact forces. b) Simulation and prototype of the biomimetic HMAs with flexible mechanoreceptive sensors. c) Stereolithography for the fabrication of actuators. d) Exploded view of the actuator body. e) Fabrication process of the flexible capacitive sensors including I) beginning with blank polyethylene terephthalate (PET) substrates, II) inkjet printing for conductive Ag nanoparticle electrodes, III) direct ink writing (DIW) printing for microstructured silicone dielectric layers, IV) repeating (II) for the top electrode, and V) aligning and bonding to form a complete sensor. f) Exploded view of the flexible capacitive mechanoreceptive sensor.

identify both transient and steady-state contact forces and can also trace the absolute readings in Newton.

These sensors are also fully printed using an entirely direct-writing style without molding, which combines inkjet printing and DIW 3D printing, used for the silver nanoparticle conductive electrodes and the silicone microstructured dielectric layer, respectively, with the complete fabrication process shown in Figure 1e. First, a 50 μm thickness PET substrate is hydrophobic treated and mounted on the workbench of a microelectronic printer (Shanghai Mifang Electronic Technology Co., Ltd.). Then, a conductive layer, serving as the electrode, is inkjet printed on the PET substrate by squeezing reactive silver nanoparticle droplets out of a 20 μm piezoelectric nozzle, followed by baking on a hotplate at 150 °C for 20 min. After the silver electrode is fully cured, the sample is replaced on the printer workbench, and insulating silicone is patterned on the silver electrode

as arrays of microscale meander lines by DIW printing using a 0.16 mm diameter syringe needle with a pressure of 100 kPa and at a speed of 1 mm s^{-1}. This silicone ink is a transparent viscous fluid with a measured viscosity of 15 Pa s, which is then baked at 80 °C for 2 h. Finally, the first step of fabrication is repeated to obtain another electrode on a blank PET substrate, which is then flipped, aligned, and bonded to the silicone dielectric layer. Thus, a flexible, bendable capacitive force sensor is fabricated, as shown in Figure 1e,f, and can be embedded on the rigid segments of an actuator as a mechanoreceptor.

The possibility of fabricating the mechanoreceptive sensors with sensitivity-enhancing microstructures using an entirely molding-free method also lies in the careful ink preparation process in addition to the 3D printing technology. **Figure 2**a shows the preparation and curing process of the silicone ink. A solution is first obtained by mixing hydroxy-terminated polydimethylsiloxane

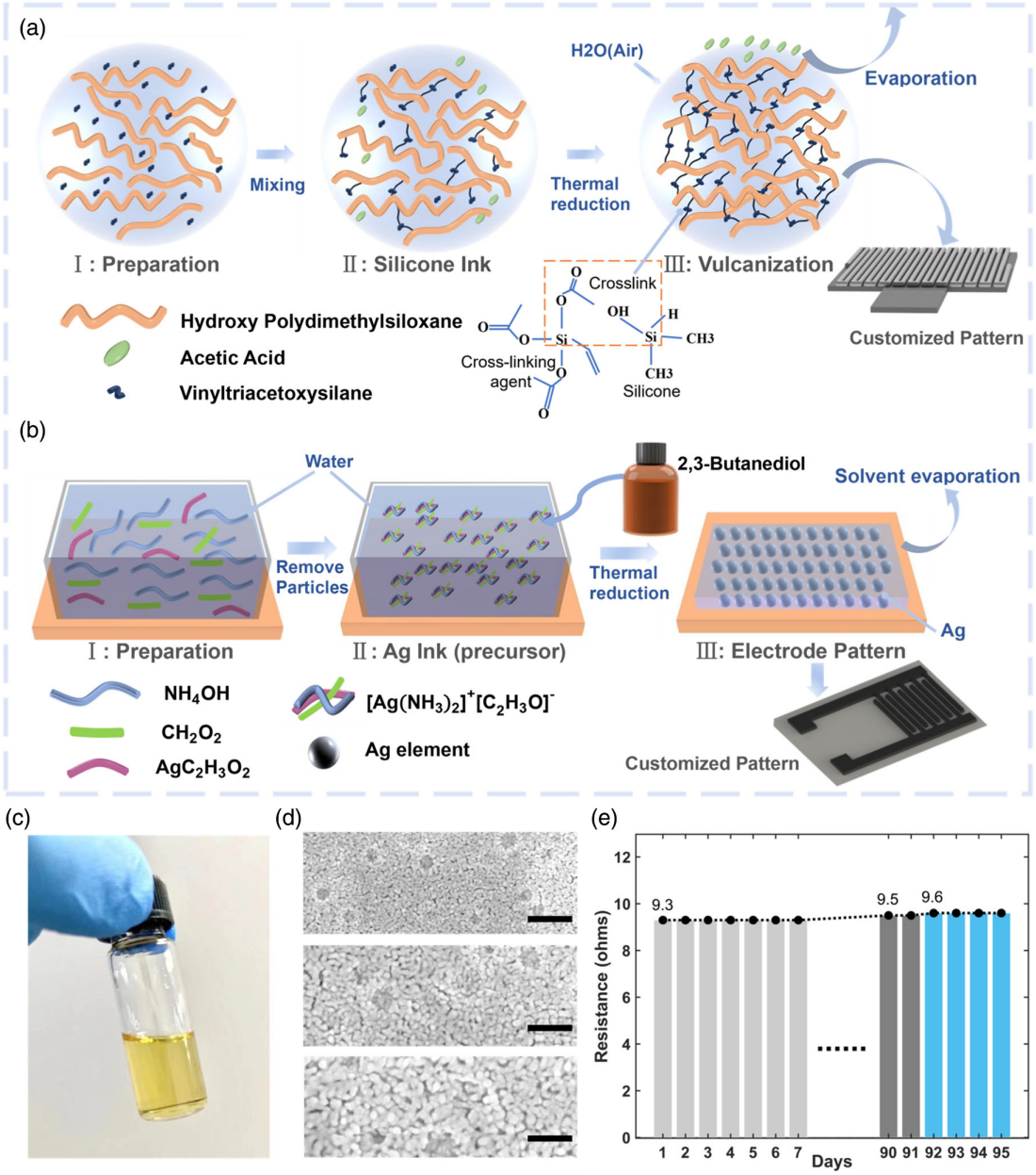

Figure 2. Ink preparation, printing, and characterization. a) The silicone-based ink is obtained by mixing cross-linking agent, vinyltriacetoxysilane, with hydroxy polydimethylsiloxane (PDMS), and then patterned by DIW 3D printing to a customized shape, followed by thermal curing. b) Printable Ag nanoparticle ink is prepared by mixing reacting silver acetate, ammonium hydroxide solution, and formic acid, and patterned by inkjet printing and thermal reduction, to form a customized electrode geometry. c) Photo of the inkjet printable transparent Ag nanoparticle ink in a scintillation vial. d) Scanning electron microscopic images of the printed Ag electrode showing densely packed conductive nanoparticles, at magnifications of 30, 50, and 80 k with the scale bars indicating 0.33, 0.20, and 0.125 µm from top to bottom. e) Stability test for the resistance of the printed Ag electrode spanning more than three months, showing excellent stability.

(PDMS) with a cross-linking agent, vinyltriacetoxysilane, for improved shape retainability of the printed structures as the interaction between the cross-linking agent and silicone chain causes an increase in the viscosity. Heating is then applied to accelerate the vulcanization of the soft dielectric layer by promoting the evaporation of acetic acid produced during cross-linking. In the end, a soft dielectric layer in a meander-shaped pattern is obtained, with a dielectric constant of 2.96 (low frequency). In contrast, Figure 2b shows the ink preparation and printing processes for the conductive electrodes. The printable ink is obtained as the clear supernatant (Figure 2c) by reactively mixing silver acetate, aqueous ammonium hydroxide, and formic acid, followed by mixing with 2,3-butanediol (10% by volume) as a humectant and viscosifying aid. This preparation process can yield a long-term stable ink and can also prevent agglomeration of the silver nanoparticles during inkjet printing if an optimized custom ejection waveform is applied to the piezoelectric. After printing and heat treatment, the organic solvent evaporates and silver particles rapidly form, resulting in a highly conductive layer with a volume resistivity around 3–10 μΩ cm. A customized electrode pattern can be easily obtained using computer-aided design software, which is implemented during inkjet printing. Figure 2d shows the scanning electron microscopic images of printed silver electrodes at 30, 50, and 80 k magnifications, demonstrating densely packed silver nanoparticles with an average size less than 20 nm. We also perform stability test of the inkjet-printed silver electrodes by tracking the resistance of a 10 × 10 mm square electrode for a sufficiently long period of time. Figure 2e illustrates an almost constant resistance from newly printed up to 95 days for a typical electrode, which is left in ambient environment, showing its excellent stability.

A large-scale manufacturing of these sensors on a single flexible substrate is easily achievable as shown in **Figure 3**a, with insets showing a better view of the transparent silicone dielectric meander arrays for one typical device. It only costs several minutes to print one sensor including the silver nanoparticle electrodes and the microstructured silicone dielectric layers, with couple of extra hours for curing, during when many new sensors can be printed. We also use a surface scanning profilometer to characterize the DIW-printed silicone structure by measuring across several ridges, revealing a micro-dome cross-sectional shape with a footprint of 0.5 mm and a height of 20 μm (Figure 3b). Such a structure would yield a similar response to received pressure as those sensors with microstructured pyramids and domes obtained by molding. Specifically, it is easier to compress the micro-domes initially for a low pressure, resulting in a high sensitivity to slight contact force, and in contrast, for the higher pressure range, if those domes have already been compressed into a flat top surface, it would become precipitously difficult to continue compressing them, resulting in a much lower sensitivity to heavy contact force, as illustrated in Figure 3c. This response is also confirmed by experimental measurement of the capacitance–force relationship as shown in Figure 3d, with two linear regimes clearly visible. The high-sensitivity regime for the small forces is measured to be $0.0538\,\mathrm{N}^{-1}$, or equivalently $0.538\,\mathrm{kPa}^{-1}$, which is high enough to detect a slight pressure change, such as the weight of leaves and potato chips. The low-sensitivity regime maintains a linear response up to 20 N (or equivalently 200 kPa), which is much larger than most other related works in literature. This highly nonlinear capacitance–force relationship is quite similar as human tactile sensation as people can easily sense a gentle touch (higher sensitivity for lower contact force) but cannot distinguish slight changes in higher pressures (lower sensitivity for large contact force). In addition, this sensor also shows excellent long-term durability, which is proved by a small change, less than 5%, after 2,500 loading–unloading cycles of a contact force between approximately 2 and 20 N (shown in Figure 3e). This accelerated lifetime test implies that the stability of this sensor would be even better for small contact forces.

2.2. Kinematics and Grasping Performance

To guide our design to enhance the output force for improved mechanical performance, we then study the kinematic model of the proposed actuator to find an analytic relationship among the inflated air pressure, the bending angle, and the output force at the tip of the actuator. Here, we utilize a plate model to analyze the deformation of the elastic tube, which can be hypothetically cut along its longitudinal axis and unwrapped into a thin plate, and thus the deformation of the elastic tube can be converted into the deformation of a plate. As shown in **Figure 4**a, the geometric parameters of the soft tube (length L, outer diameter D, and inner diameter d) are converted to an equivalent thin plate (length L, width $C = \pi D$, and thickness $t = (D-d)/2$). Under inflation, the longitudinal stress of the plate along the three perpendicular directions are σ_l, σ_c, and σ_t, respectively, while the correspondent strained dimensions along these three directions are $L' = L + \Delta L$, $C' = C + \Delta C$, and $t' = t + \Delta t$, with the stretching ratios λ_L, λ_C, and λ_t, respectively, defined as

$$\lambda_\mathrm{L} = \frac{L'}{L},\ \lambda_\mathrm{C} = \frac{C'}{C},\ \lambda_\mathrm{t} = \frac{t'}{t} \tag{1}$$

Due to the volume conservation of elastic materials, we will have $\lambda_\mathrm{L}\lambda_\mathrm{C}\lambda_\mathrm{t} = 1$. Because the rigid frames can restrict radial expansion, the stretching ratio along the width direction must ensure $\lambda_\mathrm{C} = 1$, resulting in $\lambda_\mathrm{L}\lambda_\mathrm{t} = 1$. When an air pressure P is applied, a bending moment is caused by the constrain layer with a moment arm length l, and can be expressed as $M_\mathrm{e} = PSl$, in which S is the inner cross-sectional area of the soft tube.

Figure 4b shows the measurement scheme for the actuator bending angles under different air pressures and also the effect of the Rigid Frame 2, which separates actuator bending into three continuous sections with angles θ_1, θ_2, and θ_3, respectively. It is well known that when bending, half of the tube is under compressive stress while the other half under tensile stress. With a tube bending angle of θ and a length of L, the stretched half increases to a length of $L + \theta D/2$, while the compressed half reduces to $L - \theta D/2$. Based on the correspondent equivalent plate model and the relationship $\lambda_\mathrm{L}\lambda_\mathrm{t} = 1$, the stretching ratios along the thickness direction can be calculated as

$$\lambda_{\mathrm{t}1} = \frac{L}{L + \theta D/2},\ \lambda_{\mathrm{t}2} = \frac{L}{L - \theta D/2} \tag{2}$$

Because tube thickness changes for different halves during the bending process, which causes an approximately elliptical inner

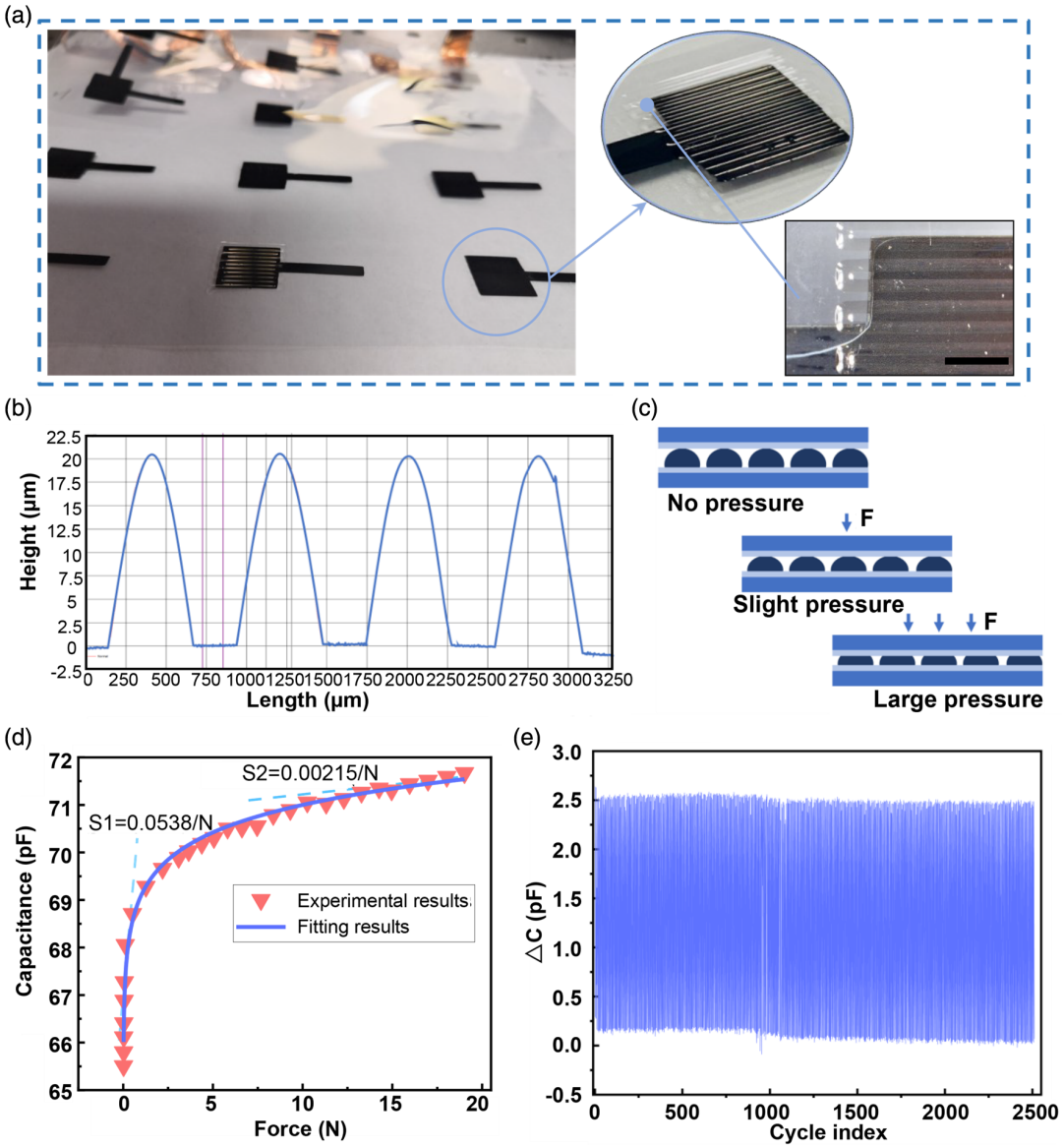

Figure 3. Characterization of the fully printed flexible mechanoreceptive sensors fabricated by 3D printing. a) Large-scale manufacturing of sensors on one PET substrate, with the insets showing the functional microstructured silicone meander arrays. The scale bar indicates a length of 2 mm. b) Surface profile of the silicone functional microstructure for one typical device showing periodic arrays of ridges for sensitivity enhancement. c) Schematic diagram of silicone deformation under no pressure, slight pressure, and large pressure, respectively. d) Measured capacitance–force relationship up to 20 N, showing two linear regimes. e) Long-term durability test of the sensor for 2,500 cycles of periodic loading and unloading a large force range from 2 to 20 N.

section's cross-sectional shape. Figure 4c shows the elliptical major axis and minor axis as $2a$ and $2b$, respectively, while the cross-sectional center offset distance e can be easily found as

$$e = \frac{(1-\lambda_{t1})t - (\lambda_{t2}-1)t}{2} \tag{3}$$

This offset distance e causes a change in the length of the moment arm from l *to* $l' = l + e$.

To find the moment after bending by $M_e = PS'l'$, we now only need to calculate the area, S', of the distorted inner shape of the soft tube. This could be accurately obtained by deleting the cross-sectional area of the tube from the inner area of the rigid frames as

$$S' = \frac{1}{4}\pi D^2 - \frac{V}{L + \theta D/2} \tag{4}$$

in which V is the initial volume of the soft tube (derivation steps in Section IV, Supporting Information). Since the constrain layer will produce a mechanical restoring moment M_c to balance the bending moment, we must have $M_c = M_e$ for equilibrium. Therefore, the relationship between applied pressure P and bending angle θ of the actuator can be calculated by the well-known 1D beam theory[42] as

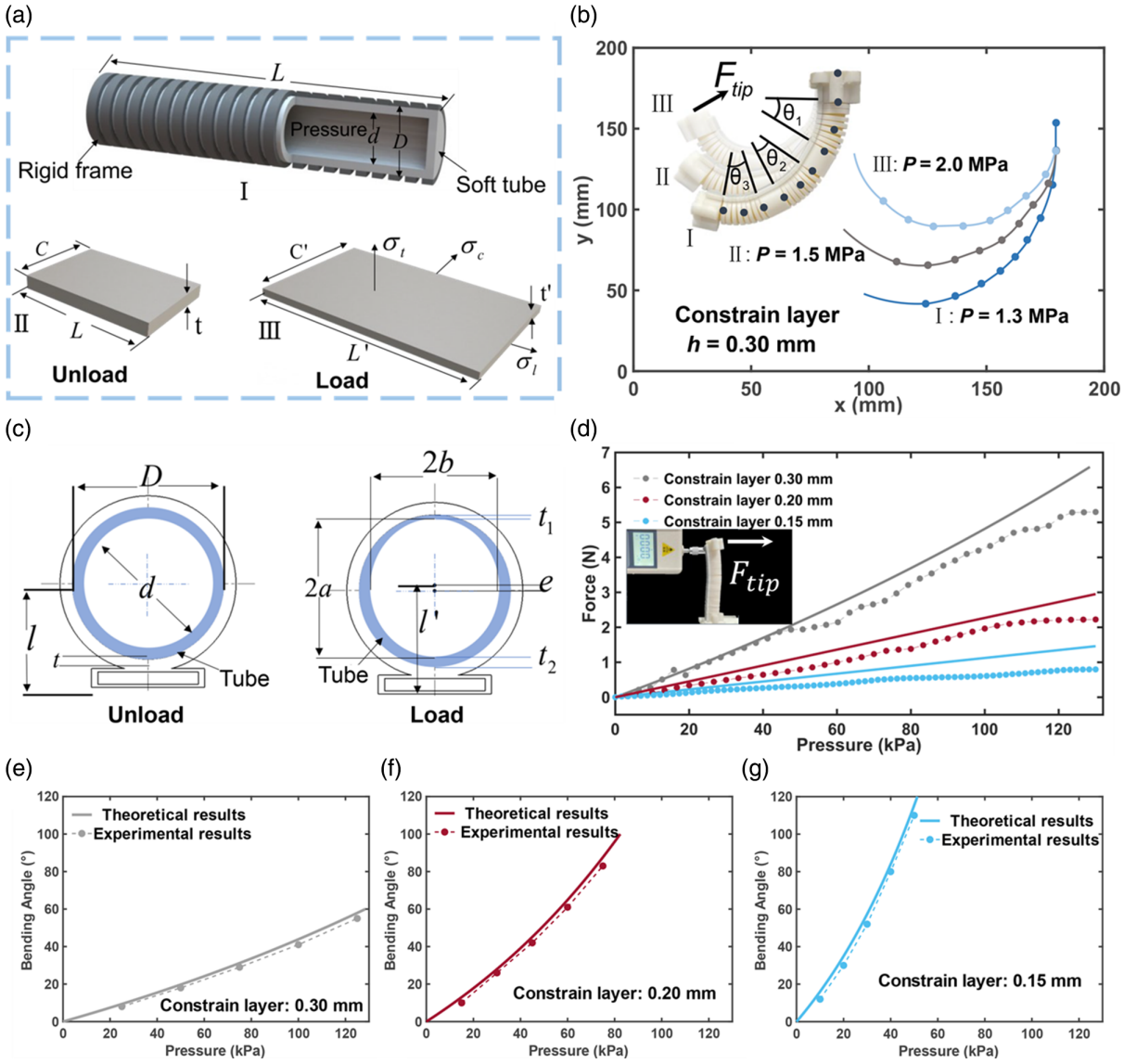

Figure 4. Kinematic modeling and actuation performance of the HMA. a) Equivalent plate model of the soft tube under pressure. b) Displacement and bending profiles of HMAs (constrain layer thickness at 0.30 mm) under different air pressures, including both experimental marker points and fitted curves. c) Cross-sectional view of the soft tube (indicated in blue) before and after deformation due to an applied air pressure, showing a change from a circular ring to an elliptical ring. d) Measured output force at the tip of the HMA as a function of pressure for different constrain layer thicknesses at 0.15, 0.20, and 0.30 mm (shown with scattered data points), with the theoretical results in solid curves. e–g) Both measured and theoretical bending angles of the HMAs as a function of pressure for different constrain layer thicknesses (0.30, 0.20, and 0.15 mm from left to right).

$$M_c = \frac{bh^3 E\theta}{12L} = M_e = PS'l' \tag{5}$$

$$\theta = \frac{12LS'l'}{bh^3 E} P \tag{6}$$

in which h and b are the thickness and width of the constrain layer (65Mn), respectively. The tip force (Figure 4d), also known as the blocking force, can be also calculated according to the same spirit as (more details in Section IV, Supporting Information)

$$F_{tip} = \frac{3M_c}{2L} = \frac{3PS'l'}{2L} \tag{7}$$

We then performed several experiments to verify the theoretical model of the fingertip force and the bending angle for our proposed actuator structure. Figure 4d shows the measured tip force F_{tip} (in scattered circles) using a force gauge as a function of pressure P for three different constrain layer thicknesses (0.15, 0.20, and 0.30 mm), with the curves representing the theoretical values. The fingertip remains in contact with the force gauge during the whole testing process, while a modest buckling in the actuator body under sufficiently high air pressure is

observed, which causes fluctuations and slight mismatch with theory for the measured results. Compared with common soft actuators consisting of pneumatic networks,[43] the output force of the proposed HMAs, reaching more than 5 N under 120 kPa, is greatly enhanced with a soft–rigid hybrid structure. Figure 4e–g shows the measured bending angle as a function of pressure for three different constrain layer thicknesses (0.15, 0.20, and 0.30 mm), showing that the bending angle increases steeply with a reduced constrain layer thickness (reduced stiffness) under the same pressure, which also matches well with our analytical model. This experiment-verified model could guide us to optimize our design to enhance the output force so that heavy working loads would be possible to achieve. Therefore, a 0.30 mm constrain layer is selected for the experiments described later, to enhance the grasping force.

We now study the grasping performance of the proposed HMAs by assembling several of them together to form a mechanoreceptive flexible gripper. We first show the inflated bending of a single HMA consisting of a combination of Rigid Frames 1 and 2. **Figure 5**a(I) shows the bending of one HMA without using any Rigid Frame 2 (longer rigid segments), which features an almost continuous bending curve. To enhance the actuator's stiffness and also provide a relatively long rigid platform to carry the mechanoreceptive sensors, Rigid Frame 2 is added to serve as an undeformed rigid segment, resulting in a discontinuous bending curve when inflated, as marked with the blue connected line segments (resembling phalanges) and dots (resembling joints) in Figure 5a(II). It is also free to change the length, location, and number of Rigid Frame 2 so that it can be custom-designed to fit the shape of particular objects, as illustrated by the example in Figure 5a(III). To demonstrate an excellent grasping performance even with a discontinuous bending of our actuators, we then assembled several of the HMAs onto a base so that a flexible gripper with mechanoreceptors is fabricated to handle various daily objects. Figure 5b shows gripper assemblies of different number of HMAs, varying from two fingers to four fingers, which are used to grab various objects of irregular shapes and distinct stiffness, such as a crispy chip, a delicate raspberry, a resin lattice, a donut, a breadboard, a heavy ball, a full water bottle, and a glass jar. The successful handling of these objects without damage or slipping demonstrates excellent adaptability to shapes, stiffness, and surface textures, partially due to the humanoid discontinuous bending and partially due to the available precise grasping force readout, which will be shown in detail

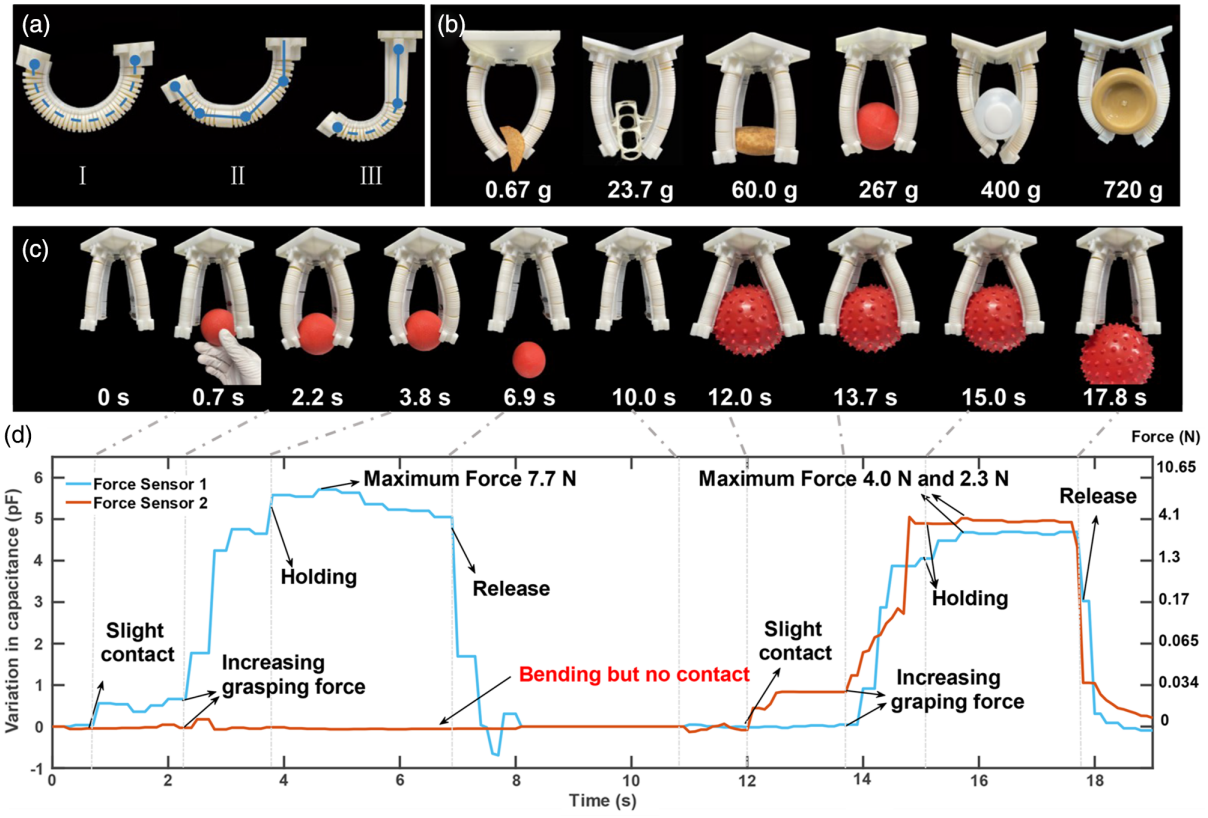

Figure 5. Grasping with mechanoreceptive feedback of the HMAs. a) Different bending conditions of the HMAs with no Rigid Frame 2 (I), and with two pieces of Rigid Frame 2 (II), and also with one long piece of Rigid Frame 2 at the anchor (III). b) Grasping of various everyday objects by soft grippers assembled with different numbers of HMAs, ranging from delicate and light-weighted to sturdy and heavy-weighted objects, including a potato chip, a raspberry, a resin lattice, a donut, a breadboard, a heavy ball, a full water bottle, and a full glass jar of peanut butter. c) Images of an interaction sequence between two balls with different weights and sizes and a gripper comprising four HMAs. d) Mechanoreceptive signal feedback, involving both the capacitance change and contact force, during the interaction process between the small ball (or big ball) and the HMA-based gripper, for five sections including an initial no-contact status at 0 s (or 11 s), a slight contact at 0.7 s (or 12 s), an increase in grasping force at 2.2 s (or 13.7 s), a holding status at 3.8 s (or 15.0 s), and finally releasing at 6.9 s (or 17.8 s).

in Section 2.3. Furthermore, this soft–rigid hybrid actuator can also handle objects spanning more than three orders of magnitude in weights (from 0.67 to 720 g), because of the stiffness enhancement for the soft–rigid hybrid design predicted by the analytical model.

2.3. Multifunctional Mechanoreceptive Feedback

For the achievement of the aforementioned successful handling of both delicate and sturdy objects, precise mechanoreceptive feedback is critical. Later, we demonstrate the advantages of force sensing and multifunctional mechanoreception of the proposed HMAs. Two flexible capacitive mechanoreceptive sensors are embedded in two long rigid frames separately to provide grasping force readouts as Sensor 1 located right at the fingertip and Sensor 2 located closer to the middle of the finger (Figure 1b), which is correspondent to human mechanoreceptors located at two neighboring rigid segments on both sides of the DIP joint (namely, the distal phalanges and the intermediate phalanges). Just like the capability of judging the pressure, size, weight, and stiffness of objects in contact with our fingers without the help of vision in everyday life, we can also determine the grasping force and estimate the size, weight, and stiffness of different objects by analyzing the sensor readouts from the HMAs. Figure 5c shows the complete mechanoreceptive grasp and release process for two objects of different size and stiffness using the same HMA. This process can be divided into five stages in time sequence: 1) the gripper initially has no contact with the object; 2) the fingertip of the gripper gets in touch with the object; 3) the gripper gradually holds the object tighter by increasing air pressure; 4) the gripper holds the object tight and still; and 5) the gripper releases the object by removing air pressure.

The first object is a small solid ball with a flat outer surface and a relatively large weight of 267.4 g. We monitor the readouts of the two mechanoreceptive sensors simultaneously during the complete process, as shown in Figure 5d. We note that this ball does not contact with Sensor 2 during the whole process due to its small size. Therefore, the output signal of Sensor 2 is almost constantly zero between 2 and 8 s (indicated by a red arrow) even when the flexible gripper finger is bending, which proves that the capacitance reading is insensitive to finger bending and will output a nonzero signal only if there is grasping pressure, thanks to the proposed FOR design. This proves that the FOR design minimizes the interference from sensor bending or potentially stretching, providing a possible pathway to overcome the well-known problem of coupled pressure response and bending responses for a typical flexible pressure sensor. For Sensor 1, the value of its output force is initially zero when the gripper has no contact with the object yet (first stage), and then the contact force reading increases slightly by approximately 0.2 N due to a gentle touch (second stage). At the third stage, the grasping force surges quickly to more than 7 N in less than 2 s as we inflate the gripper. And then at the fourth stage, the gripper holds the object by a steady-state contact force of 7.7 N (air pressure 130 kPa) without any slipping. Finally, the grasping force returns to zero after the ball was dropped by removing the applied air pressure. The release stage shows that the sensor response is on the order of tens of millisecond to sub-second, and clearly proves its fast responsiveness and capability for monitoring quick transient pressure changes.

The second object in this experiment is a larger but light-weight plastic ball (69.9 g) with a spiky surface. We repeated the same grasp and release process and recorded the sensed contact force of the two sensors. First, both sensors maintained its initial capacitance value (zero force) before contacting the object. After we snugged the ball inside the gripper, it could stay there without even applying air pressure to the actuator because of its larger size. Interestingly, the output force of the Sensor 1 kept at zero while the force of the Sensor 2 increased slightly by about 0.3 N, which is opposite to the response when we used the first object. This is because the fingertip (where Sensor 1 locates) does not contact with the larger ball while only the middle part of the fingers (where Sensor 2 locates) are used to hold it. Then, at the third stage, the contact force of both sensors increases quickly as the gripper holds tighter. At steady state, the maximum contact forces are maintained at around 2.3 and 4.0 N for Sensor 1 and Sensor 2, respectively, correspondent to a pressure level of about 130 kPa. Due to its lighter weight, the grasping force is much lower comparing to the first object, although the spiky plastic ball is larger. Finally, the ball was dropped and both sensors returned to the initial zero force status. We note that the holding force of the first object decreases slightly comparing to the stable contact force holding the second object, which is due to some slight sliding of the first object during the fourth stage because the applied grasping force is a little from enough to securely clamping it.

To further demonstrate multifunctional mechanoreceptive feedback, we measured the force from the two sensors for grabbing various daily objects ranging from small to large in size and also from light to heavy in weight, as shown in **Figure 6**a. Due to the distribution of the two sensors along finger joints, size of grasped objects could be estimated based on the contacting condition along the HMA finger. The objects with small size (e.g., cherry tomato, orange, apple, and small solid ball) do not contact with Sensor 2 at all, and the objects with large size (e.g., plastic ball, dragon fruit, and peach) always contact with both Sensor 1 and Sensor 2. In addition, the grasping force is positively correlated with the weight of the object, as a larger force is necessary to hold a heavier object without slipping. This can be clearly seen by comparing the holding force of two objects, the light-weight plastic ball and the heavier but smaller peach, as the former is requiring a much smaller force though slightly larger in size. We speculate that it could potentially reveal the accurate weight and size by increasing the number of sensors along actuator fingers and analyzing a large volume of experimental data using deep learning algorithms. Furthermore, we investigated the possibility to estimate the stiffness of the grasped objects by analyzing the grabbing force–pressure relationship for a raw-shelled egg and then the same egg but boiled and without its shell, as shown in Figure 6b. This ensures measurements of almost the same weight, size, and shape but significantly different stiffness. It clearly shows that the grasped force is much larger for the stiffer-shelled egg than that of the softer boiled shell-less egg for the same amount of air pressure. Assuming the finger bending angle, thus also the finger displacement, can be inferred from the air pressure, this could imply the stiffness obtained as dividing the measured contact force by the air pressure. We could therefore estimate the stiffness of the grasped objects and also

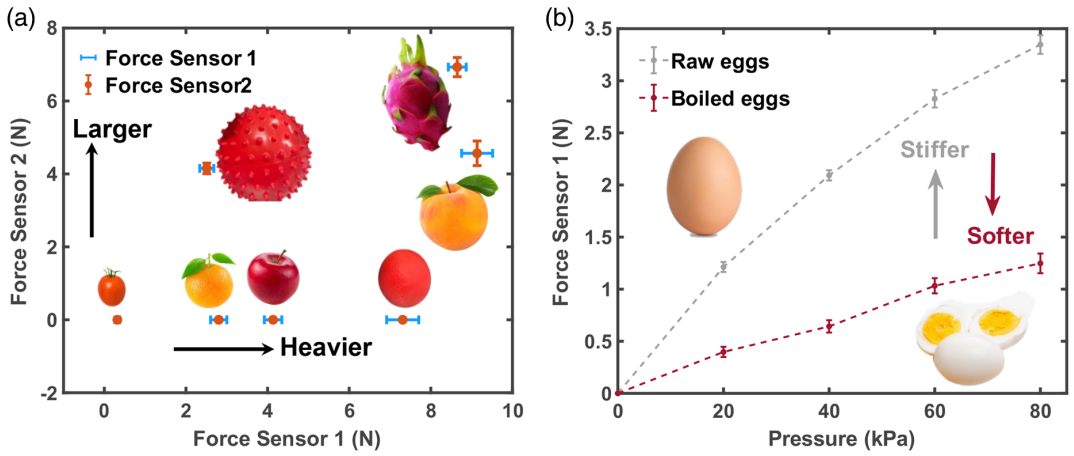

Figure 6. Multifunctional mechanoreceptive feedback of the proposed HMAs for the estimation of size, weight, and stiffness of the grasped objects. a) Measured force outputs of both Sensor 1 located at the tip of a soft robotic finger (imitating human tactile sensors at distal phalanges), and Sensor 2 located at the middle of a soft robotic finger (imitating human tactile sensors at intermediate phalanges), for grabbing a series of objects with different sizes and weights. The Force Sensor 1 is indicated in blue while the Force Sensor 2 is indicated in red. The error bars represent the +/− of one standard deviation for 10 repeated measurements. b) Measured contact force at the tip of the soft robotic finger as a function of air pressure for two objects (a shelled egg and a boiled shell-less egg) of the same size, weight, and shape but different values in stiffness. The error bars represent the +/− of one standard deviation for 10 repeated measurements.

conclude that the stiffness of the shelled egg is almost three times larger than the boiled shell-less egg. We note that considerable error would be present because the air pressure does not map to finger displacement linearly and it is worse for stiffer objects, which interfere more seriously with the finger bending process. Nevertheless, the proposed HMA provides a pathway for multi-functional mechanoreceptive sensation for soft robots as it could function like human hands to explore objects blindly for their weight, size, and stiffness.

3. Conclusion

We have shown that a multimodality all-3D-printing technology enables the construction of a fully printed soft–rigid hybrid actuator with embedded mechanoreceptors, imitating the musculoskeletal structure of human fingers with tactile sensation. The soft–rigid hybrid design not only enhances the output force, but also yields a discontinuous bending deformation, which is a closer imitation of human fingers, resulting in better grasping for objects of irregular shapes. Furthermore, this hybrid design provides rigid undeformed segments to integrate the soft mechanoreceptive sensors so that the response brought by shape deformation can be easily eliminated, which directly decouples undesired response from deformation and useful response from the received pressure. In contrast, the capacitive mechanoreceptive sensor, fabricated by an all direct-writing style of 3D printing technology, can sense the precise absolute force for both transient and static pressures with little hysteresis and long-term durability. By demonstrating grabbing and holding of various objects using the proposed HMAs, we showed soft robotic operation with multi-functional mechanoreceptive feedback as it can determine contact, handle objects with distinct weights, and also estimate size and stiffness. Our approach of preparing different inks and constructing soft robotic mechanosensation, combined with the proposed kinematic model, can provide a pathway for more accurate and agile control of soft robots.

4. Experimental Section

Design and Assembling of HMAs: The assembly process of the HMAs with different rigid frames is shown in Figure S2, Supporting Information. A number of different types of rigid frames, a soft tube, and a constrain layer were prepared beforehand. The process included the following steps. First, the soft tube was trimmed to a proper length and one end was connected to a pedestal frame for sealing. We then installed a Rigid Frame 3 outside the soft tube, with a constrain layer fixed onto it, which was used to restrict the installation of other rigid frames and constrained the bending direction of the HMA. After the constrain layer was inserted into the groove of the Rigid Frame 3, several sets of different rigid frames were installed along the constrain layer in sequence. Finally, a Top Frame was mounted to the other end of the soft tube to seal it.

Characterization of the Flexible Mechanoreceptive Sensors: The surface profile of the silicone functional microstructure was obtained using a stylus profiler (Alpha-Step D-600). The magnified imaging of the Ag electrodes was carried out using a scanning electron microscope (Tescan MIRA3). The imaging of the microstructured silicone meander arrays was carried out using a digital microscope (Keyence). The stability test of the printed silver nanoparticle electrodes was characterized by measuring the resistance along the central axis of the printed square silver electrode, using a handheld LCR (Inductance (L), Capacitance (C), and Resistance (R)) meter (Keysight U1773C). The performance of the fully printed flexible mechanoreceptive sensors was characterized using a handheld LCR meter (Keysight U1733C) to measure the capacitance and a force gauge (HP-2, Wenzhou Haibao Instrument Co., Ltd.) to record the contact force. The capacitive sensor was characterized at 100 kHz, which was tested and confirmed to be around the center of the plateau regime in the capacitance–frequency curve beforehand.

Sensitivity Improvement of the Mechanoreceptive Sensors: To enhance the sensitivity, the coverage percentage, printing linewidth, and height of the dielectric layer needed to be optimized because the deformation of the soft silicone structures directly determined the force–capacitance relationship,

thus the sensitivity of the mechanoreceptors. We therefore explored various DIW printing parameters, including nozzle diameter, pressure, speed, and height, and found that the minimum reproducible linewidth for our 15 Pa s silicone ink was 0.35 mm and better linewidth could be achieved with higher-viscosity inks and higher air pressure.[44] In addition, we also investigated the sensitivity of the capacitive sensor as a function of the coverage percentage of the silicone dielectric layer on the PET substrate with the same printing parameters, and concluded that the smaller the coverage percentage is, the higher the sensitivity would be as long as enough silicone is used to prevent capacitor shortage. This could be easily attributed to the reduced modulus of the silicone–air dielectric layer for a smaller coverage percentage. The sensor used in this work was optimized according to the aforementioned findings.

Characterization of the HMAs: The experimental setup for measuring the fingertip force is shown in Figure 4d. The HMAs were fixed at its pedestal, and a force gauge (HBO instrument HP-2) was used to measure the fingertip force, with three different constrain layer thicknesses. We used an air pump (ELUAN E8L–550W) to provide the actuation pressure and a barometer (XUNT YN60) to monitor the value of the applied pressure. The displace and bending profile of HMAs were carried out using a camera (Canon EOS 5D) by the positions of the markers.

Supporting Information

Supporting Information is available from the Wiley Online Library or from the author.

Acknowledgements

S.G. and Q.D. contributed equally to this work. Research was supported by the Shanghai Sailing Program of Shanghai Science and Technology Committee, China (Grant no. 19YF1425000), the National Science Fund for Young Scientists of China (Grant no. 12002201), and the National Science Foundation of China (Grant no. 12032015).

Conflict of Interest

The authors declare no conflict of interest.

Data Availability Statement

The data that support the findings of this study are available from the corresponding author upon reasonable request.

Keywords

bending-insensitive pressure sensing, flexible-on-rigid, multifunctional tactile sensing, soft-rigid hybrid actuators

Received: November 27, 2021
Revised: January 16, 2022
Published online: February 25, 2022

[1] J. Shintake, V. Cacucciolo, D. Floreano, H. Shea, *Adv. Mater.* **2018**, *30*, 7035.
[2] D. Rus, M. T. Tolley, *Nature* **2015**, *521*, 467.
[3] S. Kim, C. Laschi, B. Trimmer, *Trends Biotechnol.* **2013**, *31*, 287.
[4] W. Wang, S. H. Ahn, *Soft Rob.* **2017**, *4*, 379.
[5] A. Firouzeh, M. Salerno, J. Paik, presented at *2015 IEEE Int. Conf. Intell. Robot. Syst (IROS)*, IEEE, Hamburg, Germany, September 2015.
[6] J. Zhou, Y. Chen, Y. Hu, Z. Wang, Y. Li, G. Gu, Y. Liu, *Soft Rob.* **2020**, *7*, 743.
[7] Y. Wei, Y. Chen, T. Ren, Q. Chen, C. Yan, Y. Yang, Y. Li, *Soft Rob.* **2016**, *3*, 134.
[8] Y. F. Zhang, N. Zhang, H. Hingorani, N. Ding, D. Wang, C. Yuan, B. Zhang, G. Gu, Q. Ge, *Adv. Funct. Mater.* **2019**, *29*, 6698.
[9] Z. Wang, Y. Torigoe, S. Hirai, *IEEE Rob. Autom. Lett.* **2017**, *2*, 1909.
[10] U. Culha, J. Hughes, A. Rosendo, F. Giardina, F. Iida, *Biosyst. Biorobotics* **2017**, *17*, 87.
[11] M. Haghshenas-Jaryani, W. Carrigan, M. B. Wijesundara, presented at *39th Mechanisms and Robotics Conf.*, Boston, Massachusetts, August 2015.
[12] L. Liu, J. Zhang, M. Luo, H. Chen, Z. Yang, D. Li, P. Li, *Appl. Mater. Today* **2020**, *21*, 100814.
[13] A. A. Stokes, R. F. Shepherd, S. A. Morin, F. Ilievski, G. M. Whitesides, *Soft Rob.* **2014**, *1*, 70.
[14] J. Zhang, T. Wang, J. Wang, M. Y. Wang, B. Li, J. X. J. Zhang, J. Hong, *Soft Rob.* **2020**, *7*, 574.
[15] X. Liu, Y. Zhao, D. Geng, S. Chen, X. Tan, C. Cao, *Soft Rob.* **2021**, *8*, 175.
[16] H. Liu, M. Li, S. Liu, P. Jia, X. Guo, S. Feng, T. J. Lu, H. Yang, F. Li, F. Xu, *Mater. Horiz.* **2020**, *7*, 203.
[17] Y. Li, T. Ren, Y. Chen, M. Z. Q. Chen, presented at *2020 IEEE Int. Conf. Robot. Autom (ICRA)*, IEEE, Paris, France, May 2020.
[18] T. P. Chenal, J. C. Case, J. Paik, R. K. Kramer, presented at *2014 IEEE Int. Conf. Intell. Robot. Syst (IROS)*, IEEE, Chicago, IL, September 2014.
[19] K. Senthil Kumar, P.-Y. Chen, H. Ren, *Research* **2019**, *2019*, 1.
[20] H. Liu, H. Zhang, W. Han, H. Lin, R. Li, J. Zhu, W. Huang, *Adv. Mater.* **2021**, *33*, 1.
[21] C. M. Boutry, M. Negre, M. Jorda, O. Vardoulis, A. Chortos, O. Khatib, Z. Bao, *Sci. Rob.* **2018**, *3*, eaau6914.
[22] J. Byun, Y. Lee, J. Yoon, B. Lee, E. Oh, S. Chung, T. Lee, K. J. Cho, J. Kim, Y. Hong, *Sci. Rob.* **2018**, *3*, eaas9020.
[23] Q. Hua, J. Sun, H. Liu, R. Bao, R. Yu, J. Zhai, C. Pan, Z. L. Wang, *Nat. Commun.* **2018**, *9*, 244.
[24] Y. Hao, Z. Liu, J. Liu, X. Fang, B. Fang, S. Nie, Y. Guan, F. Sun, T. Wang, L. Wen, *Smart Mater. Struct.* **2020**, *29*, 35006.
[25] X. Wang, H. Zhang, L. Dong, X. Han, W. Du, J. Zhai, C. Pan, Z. L. Wang, *Adv. Mater.* **2016**, *28*, 2896.
[26] S. Liu, Y. Li, W. Guo, X. Huang, L. Xu, Y. C. Lai, C. Zhang, H. Wu, *Nano Energy* **2019**, *65*, 104005.
[27] H. Chen, Y. Song, X. Cheng, H. Zhang, *Nano Energy* **2019**, *56*, 252.
[28] J. Chen, B. Chen, K. Han, W. Tang, Z. L. Wang, *Adv. Mater. Technol.* **2019**, *4*, 337.
[29] S. Chen, Y. Pang, H. Yuan, X. Tan, C. Cao, *Adv. Mater. Technol.* **2020**, *5*, 1075.
[30] G. Yao, L. Xu, X. Cheng, Y. Li, X. Huang, W. Guo, S. Liu, Z. L. Wang, H. Wu, *Adv. Funct. Mater.* **2020**, *30*, 2070035.
[31] Y.-C. Lai, J. Deng, R. Liu, Y.-C. Hsiao, S. L. Zhang, W. Peng, H.-M. Wu, X. Wang, Z. L. Wang, *Adv. Mater.* **2018**, *30*, 1801114.
[32] X. Wu, J. Zhu, J. W. Evans, A. C. Arias, *Adv. Mater.* **2020**, *32*, 5970.
[33] R. L. Truby, M. Wehner, A. K. Grosskopf, D. M. Vogt, S. G. M. Uzel, R. J. Wood, J. A. Lewis, *Adv. Mater.* **2018**, *30*, 6383.
[34] J. H. Low, W. W. Lee, P. M. Khin, N. V. Thakor, S. L. Kukreja, H. L. Ren, C. H. Yeow, *IEEE Rob. Autom. Lett.* **2017**, *2*, 880.
[35] J. Sun, J. Zhao, presented at *2020 IEEE/RSJ Inter. Conf. on Intelligent Robots and Systems (IROS)*, IEEE, Las Vegas, NV, October 2020.
[36] Z. Liang, J. Cheng, Q. Zhao, X. Zhao, Z. Han, Y. Chen, Y. Ma, X. Feng, *Adv. Mater. Technol.* **2019**, *4*, 317.
[37] Z. Xie, F. Yuan, Z. Liu, Z. Sun, E. M. Knubben, L. Wen, *IEEE/ASME Trans. Mechatron.* **2020**, *25*, 1841.

[38] S. Lee, A. Reuveny, J. Reeder, S. Lee, H. Jin, Q. Liu, T. Yokota, T. Sekitani, T. Isoyama, Y. Abe, Z. Suo, T. Someya, *Nat. Nanotechnol.* **2016**, *11*, 472.
[39] Z. Liu, Y. Zheng, L. Jin, K. Chen, H. Zhai, Q. Huang, Z. Chen, Y. Yi, M. Umar, L. Xu, G. Li, Q. Song, P. Yue, Y. Li, Z. Zheng, *Adv. Funct. Mater.* **2021**, *31*, 7622.
[40] J.-Y. Yoo, M.-H. Seo, J.-S. Lee, K.-W. Choi, M.-S. Jo, J.-B. Yoon, *Adv. Funct. Mater.* **2018**, *28*, 4721.
[41] S. Kim, M. Amjadi, T.-I. Lee, Y. Jeong, D. Kwon, M. S. Kim, K. Kim, T.-S. Kim, Y. S. Oh, I. Park, *ACS Appl. Mater. Interfaces* **2019**, *11*, 23639.
[42] Q. M. Wang, L. Eric Cross, *J. Am. Ceram. Soc.* **1999**, *82*, 103.
[43] B. Mosadegh, P. Polygerinos, C. Keplinger, S. Wennstedt, R. F. Shepherd, U. Gupta, J. Shim, K. Bertoldi, C. J. Walsh, G. M. Whitesides, *Adv. Funct. Mater.* **2014**, *24*, 2109.
[44] H. Yuk, X. Zhao, *Adv. Mater.* **2017**, *30*, 4028.